Modeling Creep and Fatigue of Copper Alloys

G. LI, B.G. THOMAS, and J.F. STUBBINS

This article reviews expressions to quantify the thermal creep and fatigue lifetime for four copper alloys: Cu-Ag-P, Cu-Cr-Zr, Cu-Ni-Be, and $Cu-Al_2O_3$. These property models are needed to simulate the mechanical behavior of structures with copper components, which are subjected to high heat-flux and fatigue loading conditions, such as molds for the continuous casting of steel and the first wall in a fusion reactor. Then, measurements of four-point bending fatigue tests were conducted on two-layered specimens of copper alloy and stainless steel, and thermal ratchetting behavior was observed at 250 °C. The test specimens were modeled with a two-dimensional elastic-plastic-creep finite-element model using the ABAQUS software. To match the measurements, a primary thermal-creep law was developed for Cu-0.28 pct Al_2O_3 for stress levels up to 500 MPa and strain rates from 10^{-8} to 10^{-2} s^{-1}. Specifically, $\dot{\varepsilon}$ (s^{-1}) = 1.43×10^{10} exp $(-197{,}000/8.31\, T(K))\, (\sigma(MPa))^{2.5}\, (t(s))^{-0.9}$.

I. INTRODUCTION

COPPER alloys, with their combination of high thermal conductivity and relatively high mechanical strength and toughness over a wide range of temperatures, are likely the best materials for complex structural applications subjected to conditions of extreme heat flux under load. Such applications range from molds for the continuous casting of steel[1–4] to the first wall of a fusion reactor.[5–8]

Continuous-casting molds must withstand contact with molten steel and remove sufficient heat to continuously solidify a solid shell. To produce high-quality steel slabs, billets, and strip, a copper mold must maintain tight dimensional tolerances and consistent surface temperatures while being subjected to constant thermal cycling (due to both short and long liquid level changes). To be economical, it must survive many months with minimum wear while over 50,000 tons of steel is pulled through it. Most important of all, it must be 100 pct safe from complete fracture, because contact between the molten steel and cooling water (separated by only a thin layer of copper) could be catastrophic.[2] New alloys are difficult to introduce, owing to the difficulty of safely demonstrating their ability to satisfy these requirements.

The first wall of the proposed fusion reactor, ITER (international thermonuclear experimental reactor), must be designed to face both thermal and nuclear radiation from several million °C plasma. This thin wall must maintain dimensional stability and withstand stresses induced by mechanical loads and temperature gradients as well as the irradiation creep and swelling induced by the high neutron fluence.[6,7,8] Achieving and proving reliable performance of the first-wall material is a key technical challenge that may determine the feasibility of commercial fusion reactors. Despite the widespread use of stainless steel in current nuclear reactors, copper alloys are the leading candidate materials for the ITER first wall.

The accurate prediction of the mechanical behavior and lifetime of the entire structure is crucial to applications such as these. To do this requires accurate models that include a robust characterization of material properties such as the thermal conductivity, thermal-expansion coefficient, and mechanical constitutive relations. The latter includes elastic, plastic, and creep behavior and fracture toughness, crack growth, and failure prediction under a variety of loading conditions, such as fatigue cycling. Furthermore, these constants must be represented in terms of fundamental constants that are still valid in complex geometries very different from the test specimens.

This article focuses on the material properties of commercially available copper alloys, optimized for both high strength and high thermal conductivity. They include precipitation-hardened (PH) and oxide-dispersion-strengthened (ODS) alloys. Their chemical compositions, trade names, and manufacturers are listed in Table I.

Continuous-casting molds are usually made of Cu-Ag-P, Cu-Cr-Zr, or sometimes Cu-Ni-Be alloys. Oxide-dispersion-strengthened alloys are leading candidates for the first wall of ITER, owing to their superior resistance to irradiation creep, relative to the PH alloys. In both of these applications, the heat flux is on the order of 1 MW m^{-2}, the maximum operating temperature is 300 °C to 400 °C, and the stress can reach 400 MPa.

The first objective of this article is to review previous work on the property models of these four copper alloys, focusing on thermal-creep and fatigue lifetime prediction. Then, fatigue experiments at the University of Illinois are reported on, with particular emphasis on a combined modeling approach to develop and evaluate a model for thermal creep of Cu-0.28 pct Al_2O_3. The ultimate objective is to build a database of property models for these and other alloy systems that can be implemented to produce accurate models of the complete structures.

II. COPPER ALLOY PROPERTIES

Several reviews on the properties of copper alloys have been published.[5,9,10,12] The PH alloys gain their strength from precipitation hardening, where intermetallic particles

G. LI, formerly Graduate Student, Department of Nuclear Engineering, University of Illinois, is Lead Engineer in Heat Transfer and Fluid Systems Design, AEPD, General Electric Aircraft Engines, Cincinnati, OH 45215-6301. B.G. THOMAS, Professor, Department of Mechanical and Industrial Engineering, and J.F. STUBBINS, Professor and Head, Department of Nuclear, Plasma and Radiological Engineering, are with the University of Illinois at Urbana-Champaign, Urbana, IL 61801.
Manuscript submitted July 20, 1999.

Table I. Copper Alloys for High-Strength, High Heat Flux Applications

Alloy (Manufacturer)	Alloy Type	Composition (Wt Pct)
C10700[9]	Cu-Ag-P	Cu - 0.1 pct Ag - 0.008 pct P
CCZ (Kabelmetal)[10]	Cu-Cr-Zr (PH)	Cu - 0.65 pct Cr - 0.10 pct Zr
C17510 (Brush Wellman)[9]	Cu-Ni-Be (PH)	Cu - 1.4 to 2.2 pct Ni - 0.2 to 0.6 pct Be
GlidCop AL-*x* (SCM Metals)[11]	Cu-Al₂O₃ (ODS)	Cu - *x*/100 pct Al (1.02 *x*/54 pct Al_2O_3)
E.g., GlidCop AL-15 (C15715)		Cu - 0.15 pct Al as oxide particles (0.28 pct Al_2O_3)

form during cooling. They can be cast and subsequently heat treated, which is advantageous for structural components with complex geometry. The ODS alloys are strengthened by a fine dispersion of hard oxide particles. They cannot be cast, since the oxide particles would not remain uniformly dispersed in the liquid phase. Products of ODS alloys are only available in wrought form (sometimes produced by powder-metallurgy technologies) and are joined by brazing or diffusion bonding.

Zinkle reviewed the thermal and mechanical properties of copper alloys employed in high-heat-flux structural components for various thermomechanical treatments.[5] The ODS alloys Cu-Al₂O₃ and the PH alloys Cu-Cr-Zr and Cu-Ni-Be were found to have the best combination of high thermal conductivity (>350 W m^{-1} K^{-1}) and high strength (0.2 pct yield strength >400 MPa) at room temperature, as shown in Figure 1(a). The PH alloys may soften due to precipitate coarsening (overaging) and recrystallization after extended exposure to temperatures above 400 °C. The ODS alloys are resistant to both softening and irradiation creep, owing to their stable oxide particles.

Blanchet[12] investigated the thermal and mechanical properties of a variety of copper alloys, including brass, tin-copper, and aluminum-copper alloys. The thermal conductivity at room temperature and the yield strength at 300 °C are presented in Figure 1(b) for the low-alloy coppers, which have the best properties.

A. *Constitutive Relations*

A major obstacle to performing an accurate thermal-stress analysis is finding material-constitutive equations that relate stress, strain, temperature, time, and strain rate, for arbitrary loading and temperature histories over the entire range of operating conditions experienced by the material. Finite-element modeling approaches include unified elasto-visco-plastic, elastic-plastic, and elastic-plastic-creep models.[13] The choice of model dictates the nature of property reporting.

Unified constitutive models characterize the instantaneous inelastic strain-rate response of a material point under arbitrary loading in terms of evolving state variables, which include temperature, stress, and structure. They can accurately simulate the coupling between plasticity and thermal creep even up to the solidification temperature.[14] For example, an increase in the slope of the stress-strain curve during a tensile test produced by work hardening or a decrease due to recovery can be reproduced in a model by corresponding increases or decreases to a structure parameter that represents dislocation density. The unified models require many additional tests, such as stress-relaxation and variable-loading tests, to determine the parameters in the model and can be computationally expensive.
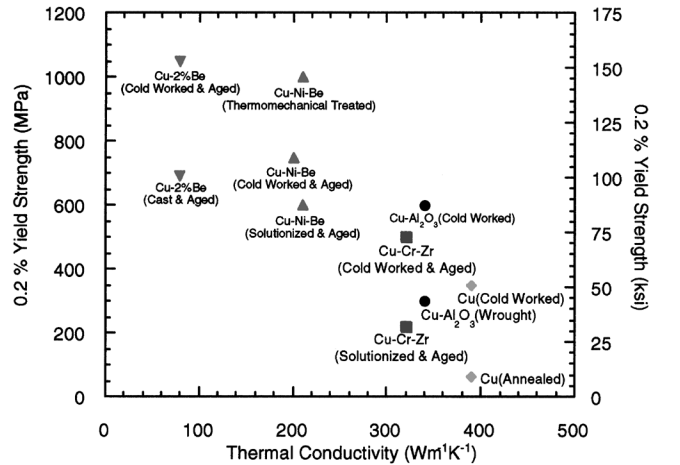
(a)
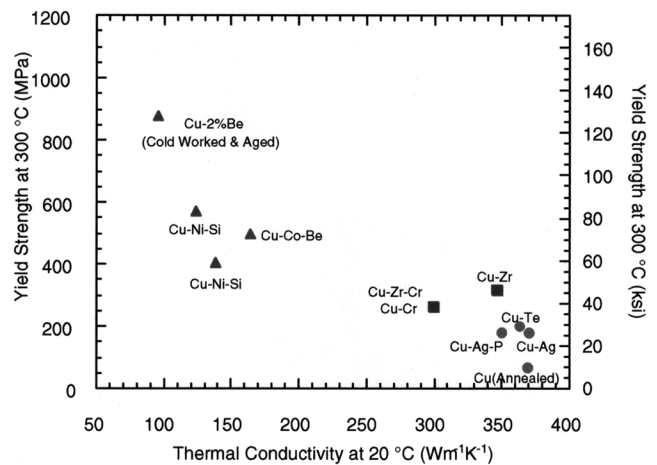
(b)

Fig. 1—(a) Strength and thermal conductivity of copper alloys (at 20 °C).[5] (b) Strength (at 300 °C) and thermal conductivity (at 20 °C) of copper alloys.[12]

Elastic-plastic models can be applied only when time-dependent plasticity and creep effects are small, or when the total strain rate is known, so that the appropriate stress-strain curves can be chosen *a priori*. Mechanical properties are extracted from standard tensile tests conducted at a constant total strain rate and are defined in terms of an elastic modulus, yield stress, and plastic modulus, all of which may vary with temperature.

When the mechanical properties depend only slightly on strain rate, an elastic-plastic-creep model is appropriate. This model splits the inelastic strain into a rate-independent plastic part and a rate-dependent creep part, which are assumed not to interact. In addition to the parameters defined in the
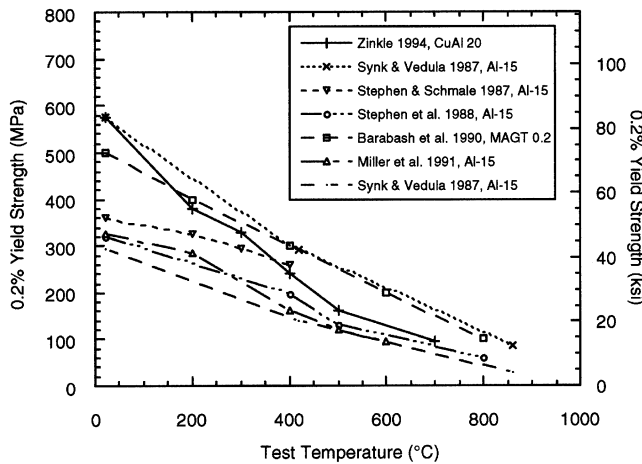
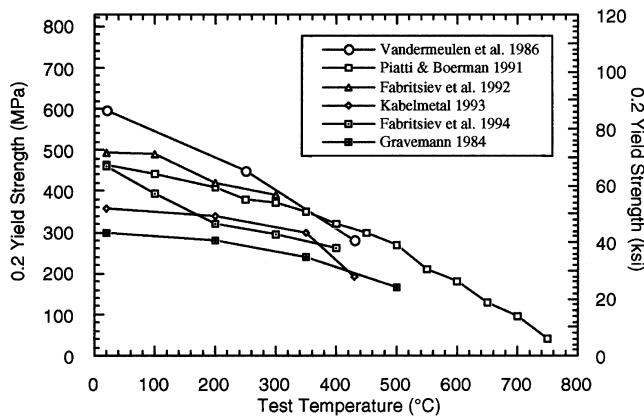Fig. 2—Temperature effect on the yield strength of Cu-Al₂O₃.[15–20] (31 to 80 pct. cold work).

Fig. 4—Steady-state thermal creep laws for copper alloys.[11,14,23–30]

Fig. 3—Temperature effect on the yield strength of Cu-Cr-Zr alloys.[5,21]

elastic-plastic analysis, a creep-strain function is needed. For high-flux structures, the plastic loading is usually small, so this approach is reasonable. For the present work, the temperature is intermediate, and measurements of copper alloys consist mainly of standard tensile tests and creep tests, which are appropriate for this model.

B. Yield Strength

The yield strength decreases steadily with increasing test temperature. The yield strengths of ODS alloys are shown in Figure 2.[15–20] Most of these data were obtained on Glid-Cop AL-15 and AL-20, which have lower strengths than the AL-25 and AL-60 alloys. The room-temperature yield strength varies between 300 and 600 MPa, mainly due to different amounts of cold work (31 to 80 pct) prior to testing.

Figure 3 shows the yield strengths of Cu-Cr-Zr alloys measured at 20 °C to 750 °C. Gravemann[21] and Kabel-metal[10] investigated the properties of Elbrodur (commercial brand) Cu-Cr-Zr, as shown in Figure 3.[5,21] The yield strength of cold-rolled Cu-Cr-Zr[22] is almost twice that of cast and aged material at room temperature, but drops faster with temperature, reaching similar strengths at 400 °C. This is because the strength increase generated by prior cold work is lost at higher temperatures due to recrystallization and
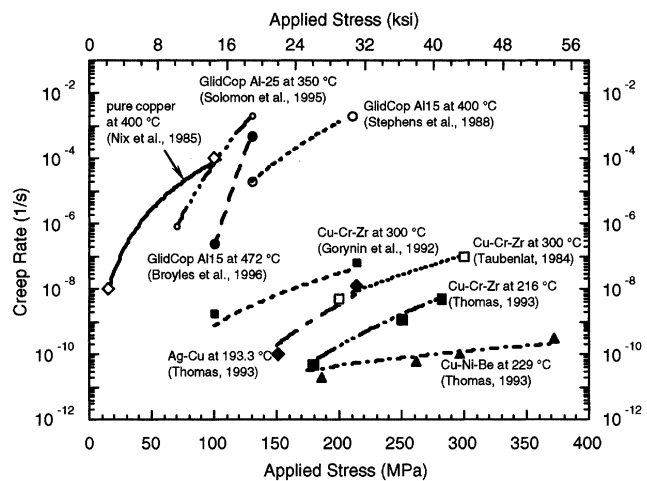
creep softening. For the same reason, the yield strengths of the silver-bearing copper alloys at room temperature are similar to the others, but they weaken rapidly when the temperature exceeds 150 °C. Thus, these nearly pure copper alloys are not as suitable for the high-temperature applications of concern in this work.

C. Thermal Creep

Models to quantify creep behavior range from simple empirical correlations, which use accumulated strain and time to characterize the material structure, to complex models, which also incorporate intrinsic material properties, microstructural features, and microstructural evolution mechanisms such as the motion of vacancies, grain boundaries, and dislocations. Creep rates are dramatically reduced by the presence of particles, particularly if they are fine and uniformly distributed, which should also be modeled.

In simulating deformation of a complex structure, it is difficult and costly to accurately predict the microstructural features and their evolution. Thus, this work adopts the common empirical relation[14] of strain rate ($\dot{\varepsilon}$), applied stress (σ), temperature (T), and time (t):

$$\dot{\varepsilon} = A \exp\left(-\frac{Q}{RT}\right)\sigma^n t^m \qquad [1]$$

where n and m are the stress- and time-hardening exponents, respectively, Q is the activation energy in kJ mol^{-1}; R (8.314 J mol^{-1} K^{-1}) is the universal gas constant; and A is a constant, with units of MPa^{n}s$^{-(m+1)}$.

This primary-creep law simplifies to a steady-state law when m is 0. The steady-state creep rate is the minimum rate measured during the second stage of a creep test.[23] It must be used with great caution when performing engineering calculations, because both primary and tertiary creep rates are much larger and potentially more dangerous.

A quantitative comparison of conventional steady-creep test data is presented in Figure 4, as a function of stress, temperature, and alloy. Selected primary-creep data are presented in Figure 5.[1,3] A curve through each set of data points was fit using Eq. [1], and the derived model parameters are presented in Table II, along with the corresponding experimental conditions. For a given material, the creep rate
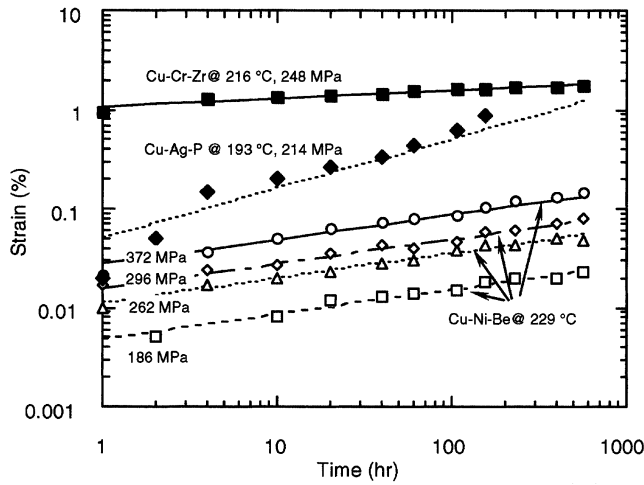
Fig. 5—Creep strain from test data and creep laws for Cu-Ni-Be, Cu-Cr-Zr, and Cu-Ag-P.[1,3]

depends strongly on the applied temperature and stress level.[11,14,23–30] In constructing the curve fits, Q and n values were adopted if they were reported, but all of the A values had to be calculated in this work.

For pure copper, the value of Q for bulk lattice diffusion (*i.e.*, vacancy diffusion) is 197 kJ mol^{-1}, and the value of n is 4.8.[25] Low-alloy copper, such as Cu-Ag-P,[1,3] exhibits similar thermal-creep behavior to pure copper, so its Q and n values are also 197 kJ mol^{-1} and 4.8, respectively. The activation energy of relatively pure copper is reported to depend on the elastic modulus E, stress exponent n, and temperature T, according to[23,25]

$$Q = -R\left(\frac{\partial \ln \dot{\varepsilon}}{\partial (1/T)}\right)_{\sigma = \text{const}} + \frac{nRT^2}{E}\left(\frac{dE}{dT}\right) \qquad [2]$$

Because E generally decreases with increasing temperature, the second term in this equation suggests that Q decreases with increasing temperature.

The dispersion-strengthened copper alloys Cu-Al$_2$O$_3$,[11,18,24,25] at high stresses and low temperatures, has

Table II. Creep Strain Experimental Data for Copper Alloys

Materials	Particle Size (μm)	Test T (°C)	Applied Stress (MPa)	Coefficient A* (MPa^{-n}s^{-m-1})	Activation Energy Q (kJ mol^{-1})	Stress Exponent (n)	Time Exponent (m*)
Pure copper[25,29]		400	15 to 105	38.8	197	4.8	0
		700					
Cu-0.001 pct Ag-0.005 pct Fe-0.015 pct O[23]	250	600	25 to 35	0.006	180	4.8*	−0.66
		350	20 to 100		180	6.6	
		400			170		
		450			155		
		500			150	4.2	
		550			135		
		600					
		650				4.2	
		700					
Cu-0.001 pct Ag[26]	210	500	35 to 65	800	186	3.8	−0.385
Cu-0.1 pct Ag-0.008 pct P[1,9]	400 to 650 anneal	193	151 to 213	1.16×10^5	197	5	−0.5
Cu-0.65 pct Cr-0.1 pct Zr[1,2,9]**		216	183 to 282	7.56×10^{11}	197	3	−0.92
				2.82×10^{-22}	197	14	0
Cu-.65 pct Cr-.1 pct Zr[4]		538		7.51×10^{12}	197	1.7	0
Cu-.45 pct Cr-0.19 pct Zr[8]		300	110 to 213	1.80×10^{-2}	197*	5.3*	0
Cu-2 pct Cr-0.3 pct Zr[27]	500 to 700 anneal	400	98	3.25×10^{-25}	134	15	0
		400	218	1.31×10^{-92}	112	41	0
		400 to 500	100 to 220		91 to 190*	15 to 41	0
Cu-2 pct Cr-0.3 pct Zr[28]	0.7	400 to 500	80 to 155		210 to 260	11 to 29	0
Cu-Cr-Zr[30]		300	210 to 300	4.64×10^{-8}	197*	7.4*	0
Cu-1.4 to 2.2 pct Ni-0.2 to 0.6 pct Be[1,9]	400 to 600 aging	229	180 to 372	1.07×10^9	197	2.5*	−0.75
Cu-Al$_2$O$_3$ (GlidCop AL-25)[11]	1000 anneal	350	70 to 130	1.28×10^{-13}	197*	12.64	0
Cu-Al$_2$O$_3$ (GlidCop AL-15)[25]	0.60	472	100 to 130	2.3×10^{-49}	257.6	30	0
	0.65	725	30 to 50	9.5×10^{-10}	248.9	10.6	0
Cu-Al$_2$O$_3$ (GlidCop AL-15)[18]		400	130 to 200	7.6×10^{-11}	197*	9.8	0
Cu-Al$_2$O$_3$[24]		650 to 850	55 to 241	—	512	15 to 22	0
Cu-Al$_2$O$_3$[24]		650	130 to 210	—	—	23 to 26	0
Cu-Al$_2$O$_3$[24]		550 to 650	17 to 27	—	368	30 to 49	0

*These values were found by fitting the referenced experimental data to Eq. [1].

**First row is a primary creep law (with a threshold stress of 159 MPa, which must be subtracted from σ before using the equation). Second row is a steady creep law (valid at times greater than the critical time when primary and secondary creep strains are equal).
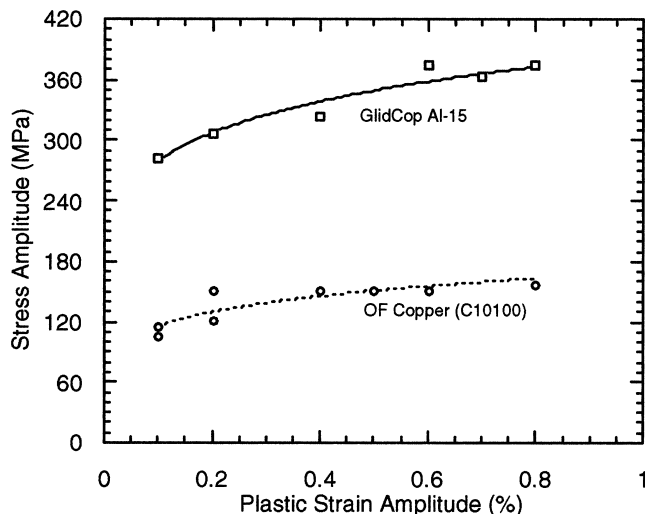
Fig. 6—Cyclic stress-strain curves of copper alloys at ambient temperature.[36,38]

n values of 4 to 8 and a Q value of around 197 kJ mol^{-1}. However, at low stresses, n increases to as high as 20 to 100, and Q reaches 3 times as high as that for bulk lattice diffusion. Also, at high temperatures, a threshold stress for ODS copper-alloy creep was reported.[28] Creep strain is negligible when the applied stress is below this threshold stress.

For Cu-Cr-Zr alloys, Q is reported to range from 100 to 197 kJ mol^{-1}, if the annealing temperature is below 600 °C.[28] For a high annealing temperature of 700 °C, Q varies widely (from 66 to 327 kJ mol^{-1}), depending on the stress and strain levels. The stress exponent n for Cu-Cr-Zr[28] increases from about 4 to 29, as the test temperature rises from room temperature to 500 °C, for stresses of 80 to 155 MPa. Beryllium copper alloys, such as Cu-Ni-Be,[1,3] have the highest thermal-creep resistance among the copper alloys studied in this work. As shown in Figures 4 and 5, its stress exponent is only 2.5.

D. *Cyclic Deformation*

Loading due to thermal cycling in a constrained region of a structure can be represented by constant strain–amplitude mechanical loading at a fixed temperature.[31,32] The plastic strain can be held constant during each cycle by controlling the instantaneously measured response. For a fully reversed, strain-controlled fatigue test, the stress amplitude decreases with time for a cyclic-softening material. This behavior is common at elevated temperatures, as creep strain due to dislocation climb and grain-boundary movement occurs during each cycle. Eventually, a stable hysteresis loop is achieved. The results of many such tests can be plotted together in a cyclic stress-strain curve, such as for the two alloys in Figure 6. Each data point is taken from a single fully reversed, strain-controlled fatigue test at ambient temperature. At high temperatures, the materials under analysis are cyclic softening, so the stress values in a constructed cyclic stress-strain plot are lower than those found in the static stress-strain curve (given in the first cycle).

In simulating the hardening or softening phenomena observed in cyclic tests, a complete constitutive model of cyclic plasticity should specifically account for (1) the Bauschinger effect, where the yield stress decreases after a load reversal, (2) cyclic-creep ratchetting, where plastic strain accumulates in each cycle of a stress-controlled fatigue test with nonzero mean stress, and (3) stress relaxation, where the stress in a strain-controlled test with a nonzero mean stress will tend toward zero with the progression of cyclic deformation. Two popular modeling approaches are "isotropic hardening," where the yield stress increases with the absolute accumulated strain, and "kinematic hardening," where the yield stress evolves and is able to reproduce Bauschinger effects and stable hysteresis loops.[33,34] This work investigates the idea that these simple time-independent elastic-plastic models, when combined with an appropriate creep law, can approximately reproduce many of the important phenomena encountered in cyclic loading.

E. *Fatigue Life*

Fatigue failure may occur in structures subjected to cyclic stresses, at stress levels considerably below the yield strength. The fatigue lifetime is lower at higher temperatures, especially when stress levels are high enough to generate significant inelastic strain in each cycle and cause low-cycle fatigue. Fatigue-lifetime-prediction models have been based on inelastic strain, total strain, stress, and other approaches. Common empirical correlations to predict fatigue lifetime include the Basquin Law,[35] the Coffin–Manson relation,[36] the Coffin–Halford formula,[37] and Neuber's rule.[35] In this work, the inelastic strain is much higher than the elastic strain, so a simplified Coffin–Manson approach[36,38] appears most appropriate:

$$\frac{\Delta\varepsilon}{2} = \varepsilon_f' \, (2N_f)^c \qquad [3]$$

where $\Delta\varepsilon/2$ is either the total strain amplitude or the inelastic strain amplitude, ε_f' is the empirical fatigue-ductility coefficient, $2N_f$ is the number of reversals to failure, and c is the empirical fatigue-ductility exponent. For an ODS copper alloy, the value of c is approximately −0.6, and ε_f' is 0.56,[29] based on the inelastic strain amplitude.

Previous work has investigated the low-cycle fatigue of copper,[31,39] copper/stainless steel or copper/beryllium welds,[40,41] oxygen-free high-conductivity copper,[42,43] and Cu-Al$_2$O$_3$,[8,31,32,40] Cu-Cr-Zr,[8] and Cu-Ni-Be alloys.[3,40] Measurements of fatigue lifetime for these copper alloys are shown in Figures 7(a) and (b). Results from recent isothermal bending experiments are given in Figure 8.[40] These results quantify the significant effect that increasing temperature has on lowering the fatigue lifetime. Fatigue-life prediction is further complicated when the loading is thermomechanical in origin, so the structure is not isothermal. For example, the failure of continuous-casting molds in service occurred after fewer cycles than predicted with an isothermal fatigue-life model.[4] The importance of these high-temperature effects in limiting fatigue lifetimes,[29,31,41] the difficulty of predicting lifetimes, and the paucity of quantitative data provide a great incentive for more work in this area.

III. FATIGUE EXPERIMENTS

Fatigue experiments were conducted on bimetallic copper/stainless steel plates. Specifically, four-point compressive
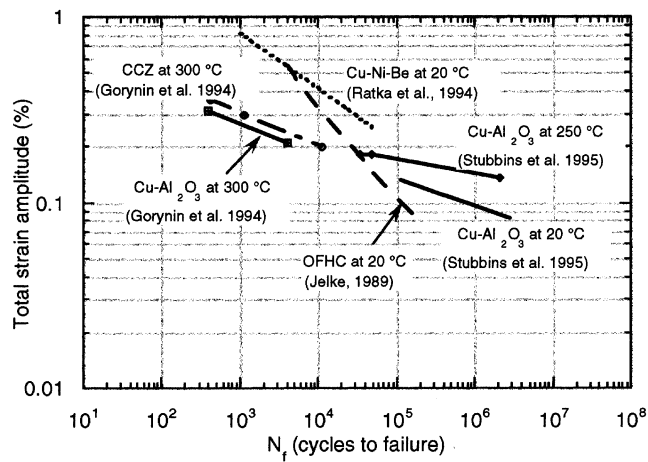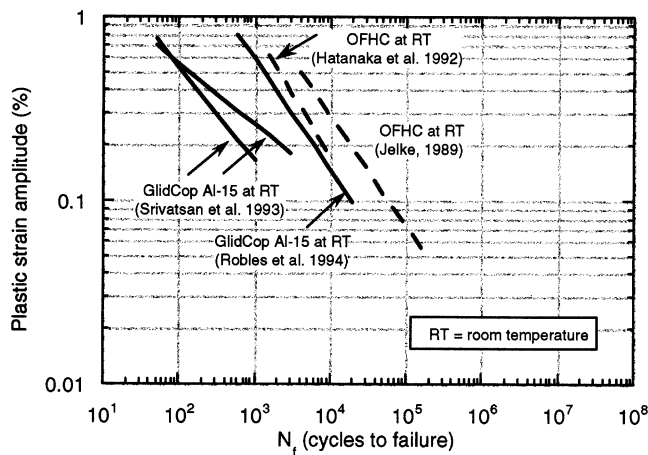
Fig. 7—(a) Fatigue lifetime of copper alloys, based on total strain amplitude.[3,6,8,42] (b) Fatigue lifetime of copper alloys, based on plastic strain amplitude.[31,32,42,43]

load and constraint conditions were applied on the bending-test specimens shown in Figure 9. The 101.6 × 12.7 × 12 mm³ specimens were made of a 6-mm-thick wrought copper alloy plate, GlidCop AL-15 (Cu with 0.28 pct Al₂O₃ particles), explosively bonded to a 6-mm-thick wrought 316L stainless steel plate. These tests were designed to approximate the geometry, fabrication methods, and loading conditions proposed for the first wall of the ITER fusion reactor. Sinusoidal loading conditions (load control) were applied with a minimum-to-maximum stress ratio (*i.e.*, *R* ratio) of 0.1. The vertical *y* displacement at the load position (point B) was recorded continuously. A summary of test conditions and results is given in Table III.

At low load, the loading and unloading curves follow the same load-displacement path during each cycle, indicating elastic behavior. Experiments performed at higher load produce large plastic strains in the first cycle, as evidenced by differences between the loading and unloading curves. Subsequent cycles follow the same path, indicating that the initial plastic strain-hardening increases the yield stress sufficiently for subsequent stresses to be entirely elastic. Experiments at higher temperatures experience inelastic strain in each cycle, indicating thermally induced creep and the phenomenon of thermal ratchetting.
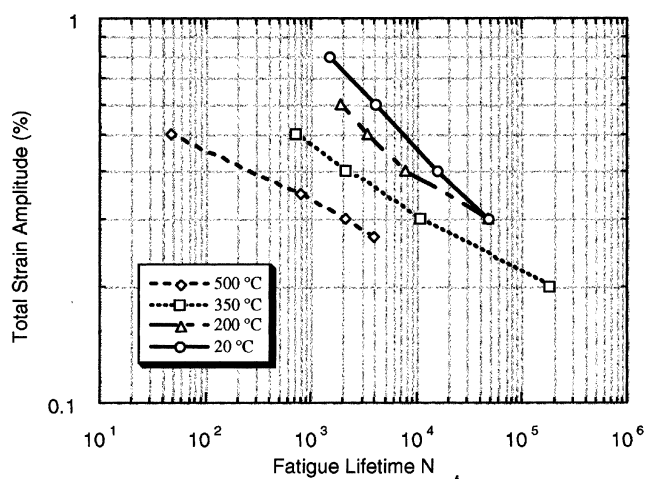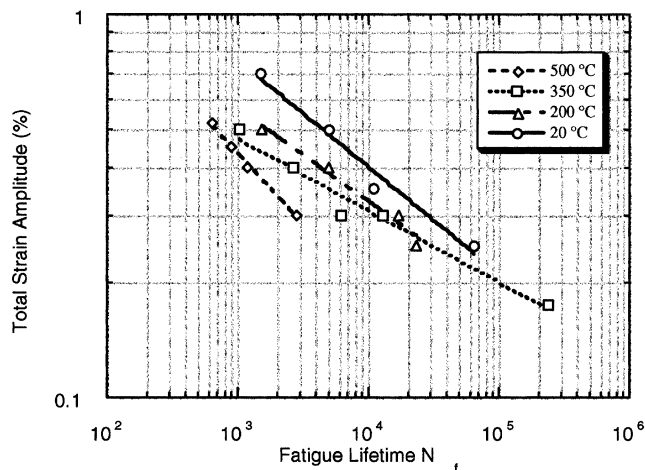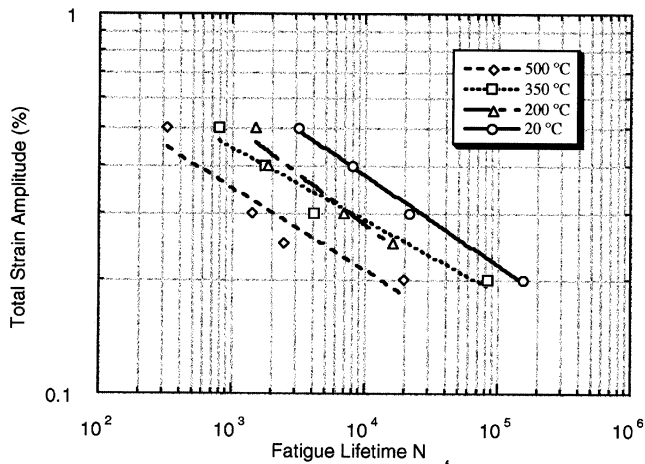
Fig. 8—(a) Temperature effect on the fatigue lifetime of Cu-Ni-Be.[41] (b) Temperature effect on the fatigue lifetime of Cu-Cr-Zr.[41] (c) Temperature effect on the fatigue lifetime of Cu-Al₂O₃.[41]

Examination of the final shapes of the test specimens found them to be distorted in two different ways. First, the bars appeared "sagged," with more deformation at the center of the specimens tested at a higher load and/or temperature.
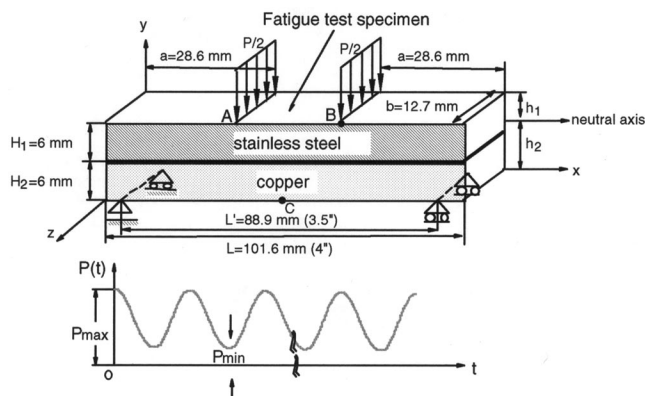
Fig. 9—Experimental specimen and four-point load conditions for bending fatigue tests.

This deformation provides evidence for the accumulation of residual plastic strains, which occur during each loading cycle. Second, each of the four points where a load or constraint was applied had a slight indentation. About 40 pct of the depth of each indentation was produced in the first loading cycle. Again, the depth increased with load and temperature. Indentations at the constraint positions in the copper were slightly deeper than at the load positions in the stainless steel, presumably because the copper is softer. Fatigue failure generally occurred at a crack perpendicular to the surface, which was initiated after a large number of cycles at the bottom copper surface. Occasional cracks turned to propagate along the interface. The crack typically grew either to or through the interface (at low loads). These results suggest that the interface bond may be stronger than the copper alloy, which deforms due to thermal creep.

IV. MODEL OF FATIGUE EXPERIMENTS

A. Finite-Element Model Description

The fatigue experiments discussed in the previous section were simulated using a two-dimensional finite-element stress model, solved with ABAQUS.[33] Since the temperature range under study is below 400 °C and property data were not available, unified models were not employed. Instead, the simpler conventional elastic, elastic-plastic, elastic-creep, and elastic-plastic-creep models were investigated. The simulation domain, load, and constraint conditions for the test-bar specimens are given in Figure 9. The model employs a 32×26 mesh of standard four-node, two-dimensional plane-strain finite elements (CPE4 in ABAQUS[33]). A mesh-refinement study revealed that further refinement increased stress predictions by less than 2 pct. Both the isotropic and kinematic hardening models give the same results, since stresses in these bending tests never exceed the yield in reverse loading. Most of the assumed mechanical properties are given in Table IV and are based on the reviewed literature for copper and stainless steel.[44] In addition, a Poisson ratio (ν) of 0.343 and a plastic modulus of 11 GPa were assumed for copper. Values of 0.283 and 8 GPa, respectively, were assumed for stainless steel.

B. Comparison with Analytical Solution and Elastic Experiments

The first simulation was conducted with a small maximum load of only 3.088 kN, to produce only elastic behavior. First, results from this elastic simulation were verified with an analytical solution (Appendix). The axial (x-stress) at the bottom center of the specimen (copper) is 221 MPa in tension, while the top (stainless steel) is about 229 MPa in compression. The neutral axis (where stress is zero) is very close to the interface of the copper and stainless steel, owing to the similarity of the two elastic moduli (130 and 140 GPa). The maximum vertical (y) displacement at the load position (point B in Figure 9) and maximum strain position (point C) are 0.13 and 0.15 mm, respectively. The compliance at point B is then 0.13 mm/3.088 kN = 4.2×10^{-8} m N^{-1}, which is the same as the analytical solution.

Next, the slopes of the elastic experimental load-displacement curves were measured. The load-extension curve in the test bar followed almost the same path during every cycle. The tiny observed changes might be attributed to small amounts of cyclic softening or hardening of the stainless steel. More importantly, the average slope of those

Table III. Fatigue Test Measurements

Specimen	Test Temperature (°C)	Maximum Load (kN)	Frequency (Hz)	Lifetime Cycles to Failure	Estimated Maximum Tensile Stress (MPa)	Indentation at Four Points (mm) Cu	SS
A-1	ambient	−7.7	*	336,401	355	*	*
A-2	ambient	*	*	>1,500,000	213	*	*
A-3	ambient	−16	*	*	450	*	*
A-4	ambient	−8.5	5	949,240	284	0.05	0.05
A-5	ambient	−8.5	5	808,470	250	0.04	0.02
A-6	ambient	−13.5	2.5	112,916	500	0.10	0.10
A-7	ambient	−6.5	5	2,766,221	225	0.03	0.02
A-11	250	−7.25	2.5	>3,000,000	250	0.08	0.02
A-12	250	−9.5	5	>6,388,821	325	0.08	0.05
A-13	250	−11.5	5	2,074,350	400	*	*
A-14	250	−13	2.5	34,876	450	0.13	0.10
A-15	250	−13	2.5	49,265	450	0.12	0.10

*Not available.

Table IV.   Material Properties

Temperature (°C)	Thermal Conductivity k (W m^{-1} K^{-1})	Thermal Expansion α (°C^{-1})	Elastic Modulus E (GPa)	Yield Stress (0.2 Pct) YS (MPa)
GlidCop AL-15				
20	344	16.6×10^{-6}	130	410
250	317	17.8×10^{-6}	130	393
Stainless steel				
20	16.0	16.0×10^{-6}	200	207
250	18.15	17.2×10^{-6}	140	200
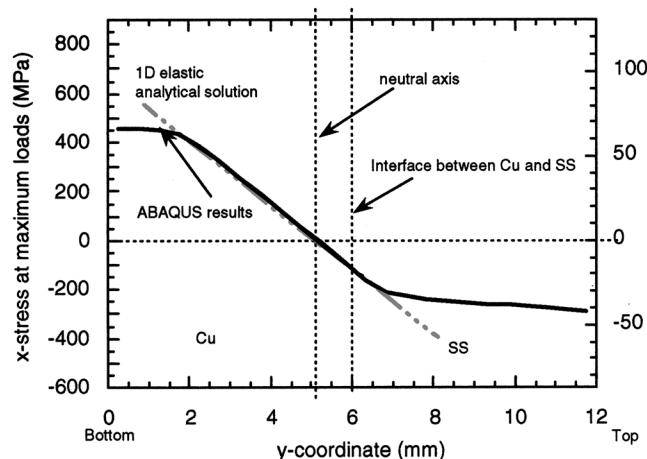
Fig. 10—Stress distribution along centerline of bending fatigue test specimen A-14 at maximum load predicted by elastic-plastic finite-element model and elastic analytical solution (250 °C).

curves matched the model predictions, indicating that the choice of elastic modulus and Poisson ratio were reasonable.

C. *Comparison with Fatigue Experiments*

Next, an elastic-plastic calculation was performed using the properties in Table IV for the conditions of test A-14 in Table III. The *x*-stress profile predicted by ABAQUS through the center of the specimen at maximum load is given in Figure 10. The top layer of the stainless steel is in compression, while the bottom layer of copper is in tension, except for a small region near the interface of the two materials. The neutral axis is displaced from the copper/stainless steel interface almost 1.0 mm into the copper. This is because the steel has more plastic strain, owing to its lower yield strength, so it supports less load. The bottom 2 mm of the copper and the top 4 mm of the stainless steel deform plastically. This naturally lowers the maximum stress levels. In the central region, the elastic solution matches the finite-element model results. The slopes in the two material zones are nearly the same, and the stress across the interface is almost continuous, owing to the similarity of the two elastic moduli.

Finally, elastic-plastic-creep simulations were conducted with the material properties presented in Table IV and were compared with the measurements. The *x*-stress and equivalent plastic-strain contours calculated at maximum lead in a typical specimen (A-14) are presented in Figure 11. As expected, high axial (*x*-direction) tension was found at the bottom of the copper alloy layer (448 MPa maximum), and high compression was found at the top of the stainless steel layer. Inelastic strains are greatest at the top and bottom surfaces.

The load was plotted as a function of relative displacement at the load position (including the local indentation effect) to compare the simulation results with the experimental record of fatigue test A-14, as shown in Figures 12 and 13(a). The slopes of the load displacement loops are related to the elastic modulus of the materials. Except for the first loop, all slopes of the load-displacement loops from the ABAQUS model match the fatigue test results. The slight underprediction of the measured displacement for the first half of the load cycle is likely due to the underprediction of the indentation and the take-up of play in the testing equipment.

The successive increases of the maximum displacement of test A-14 are attributed to thermal ratchetting, because inelastic thermal creep is significant in this copper alloy at the elevated test temperature of 250 °C. Although the 2.5 Hz frequency of this test is very fast, creep is still believed to be the dominant phenomenon. The importance of creep would be expected to be even more important, if the fatigue cycling frequency were lower. Plasticity is significant only during the first cycle and is followed by a rapid "shakedown" period. The accumulated displacement in each cycle decreases rapidly with increasing cycles. This might be due to the decrease in creep rate in the primary-creep regime.

The trends of both the predictions and fatigue test results are the same. The maximum deflection, at the center of the specimen, is 1.07 mm. This is close to the 1.0 mm measured in specimen A-14. Plastic strain is predicted to be large in the first half of the loading cycle (0.2 mm of the 0.81 mm total displacement at the load position), and then drops rapidly to reach zero in subsequent cycles. Although the test was conducted in load control, the maximum load in the first cycle did not reach the prescribed value of −13 kN. This accounts for the difference between the simulation and the measured stress after the first half of the cycle. The actual indentation in the first cycle of test A-14 is estimated to be about 0.06 mm, considering that a significant fraction of the final accumulated indentation of 0.13 mm is expected in the first cycle. The calculated depth of the indentation after the first half-cycle is 0.04 mm, which compares reasonably with the measurement, considering the course size of the finite-element mesh near the indentation. The thermal-creep law used in the simulation underpredicts the accumulated displacement at long times (large cycles) for the test at 450 MPa (A-14), while it slightly overpredicts for the test at 400 MPa (A-13). This can be seen by examining Figure 13, where each large symbol on the predicted curve corresponds to a series of smaller symbols that define the measured response at a particular selected cycle. The discrepancies correspond to the mismatch between the new thermal-creep law and the estimated creep rates, which are compared in Figure 14 and discussed in the next section.
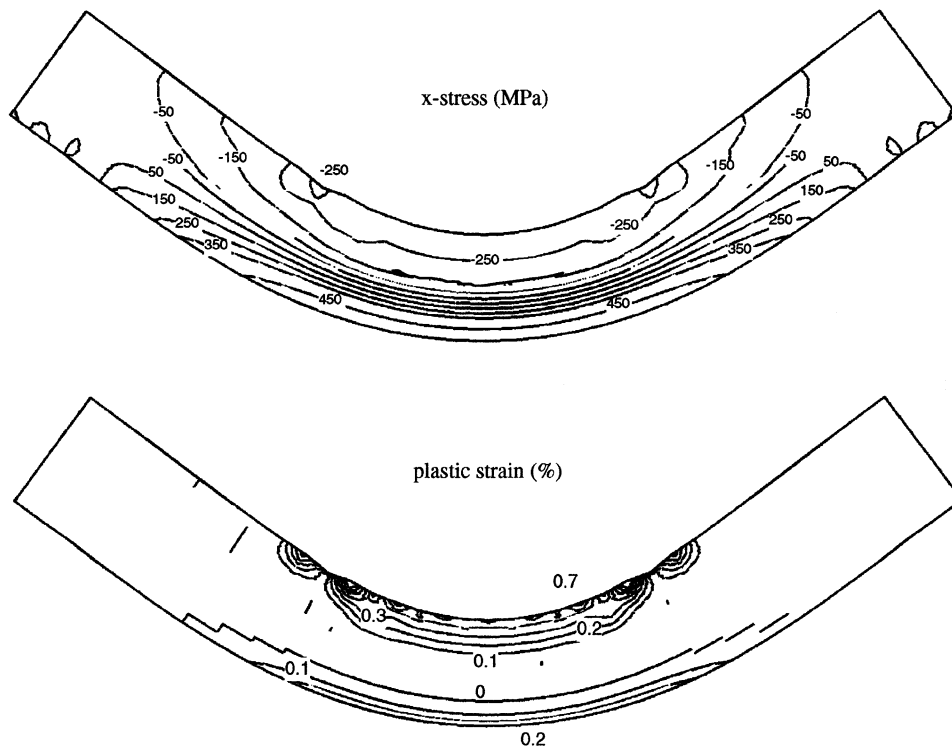
Fig. 11—Elastic-plastic-creep model predictions of *x*-stress and plastic strain distributions at maximum load (specimen A-14).
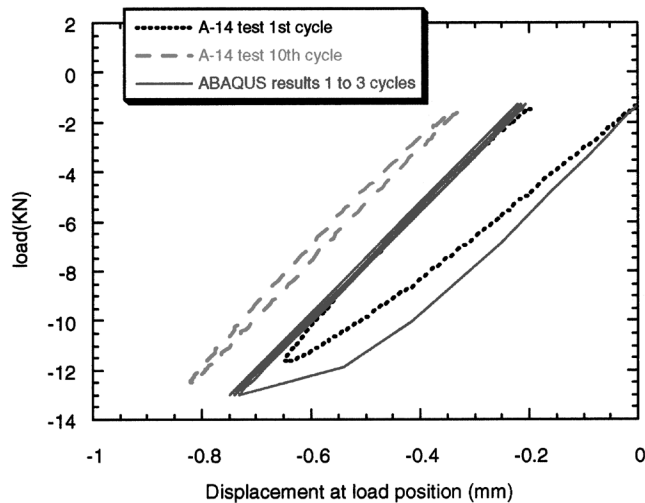

Fig. 12—Elastic-plastic-creep model prediction of raw fatigue-test measurements at early cycles (specimen A-14 at 250 °C).

V. THERMAL-CREEP LAW FOR GLIDCOP AL-15 ALLOY

No creep law was available from the literature for the GlidCop AL-15 alloy, so constants for the creep law were chosen such that the simulations described in the previous section were able to reasonably match the fatigue test measurements. This was achieved *via* the following steps.

(1) First, the load-position data recorded for the high-temperature tests A-11 to A-14 were converted to displacement-time curves, knowing the number of load cycles

and their frequency. Relative displacement was measured at the load position (point B) at the point of maximum load in each cycle. The average displacement was crudely estimated by dividing the total increase in displacement between two recorded cycles by the number of cycles between them.

(2) Next, the displacement/time curves were converted to creep-rate/time curves (Figure 14). To determine the relation between the displacement and the creep rate, the transient elastic-creep finite-element model described in the previous section was applied to simulate a single load cycle under conditions of both constant loading and sinusoidal loading. For typical test conditions, the result was that the creep strain accumulated over a complete sinusoidal cycle is the same as that for the case of a constant maximum load applied over about half of the cycle period. The exact relation is independent of load, but varies with frequency. Using the appropriate relation for each test, an input creep rate was found to match each corresponding increase in the displacement at B, so the creep-rate/time curves could be constructed. For the tests with different periods, additional linear conversion was needed to make the total creep time the same.

(3) Finally, the creep rates were paired with the average time of the two recorded cycles. Creep-rate curves for other Cu alloys are supplied on the same graph for comparison. These curves, from Thomas, *et al.*[1,2] are time-, stress-, and temperature-dependent primary creep laws for copper alloys, as given in Table II and shown in Figure 5. The stress exponent was found from the slope of ln ($\dot{\varepsilon}$) ∼ ln (σ) curves of the four 250 °C
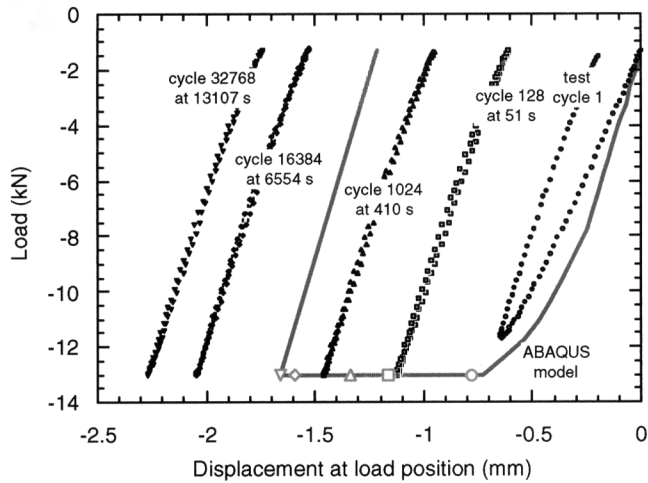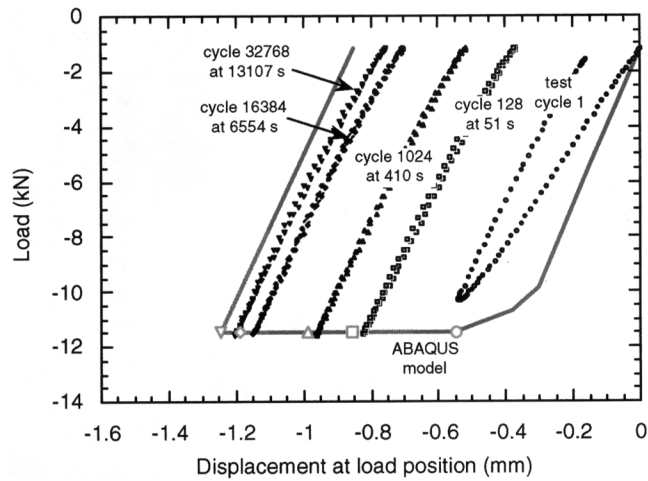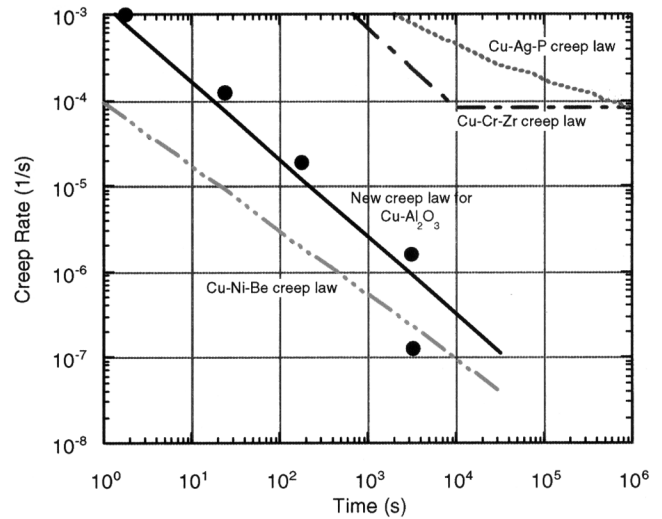
Fig. 13—(a) Elastic-plastic-creep model prediction of raw fatigue-test measurements at long cycles (specimen A-14 at 250 °C). (b) Elastic-plastic-creep model prediction of raw fatigue-test measurements at long cycles (specimen A-13 at 250 °C).
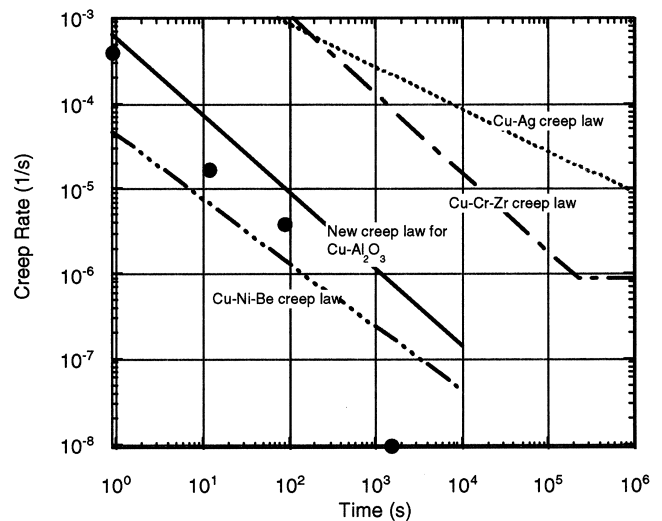

Fig. 14—(a) Copper alloy creep laws compared with A-14 test data (maximum load = 13 kN, T = 250 °C). (b) Copper alloy creep laws compared with A-12 test data (maximum load = 9.5 kN, T = 250 °C).

tests at long time. The accuracy of this calibration is illustrated in Figure 14. The new creep function for a Cu-0.28 pct Al$_2$O$_3$ alloy or Glidcop AL-15 is

$$\dot{\varepsilon} \ (s^{-1}) = 1.43 \times 10^{10} \exp\left(-\frac{197,000}{8.31 \ T \ (K)}\right)$$

$$[\sigma(MPa)]^{2.5} \ [t \ (s)]^{-0.9}$$

[4]

This simple power-law creep correlation in Eq. [4] roughly predicts the measured creep rate over this range of loads (7.25 to 13 kN), stresses (250 to 450 MPa), and times (0.1 to 10^4 s), at least at 250 °C. Figure 14 compares the constant-log slope of the power-law curve with the gradually steepening curve from the experiments. In all cases, the creep rates tend to very small values at large test cycles (long times). The small steady values expected for secondary creep were not reached in only 10^4 seconds. Creep rates predicted with the new creep law compare reasonably with those of previous creep laws, as shown in Figure 14.

VI. DISCUSSION

Four-point-bending fatigue tests were performed on layered copper-stainless steel specimens, and thermal ratchetting was observed for the tests at 250 °C. The tests were then simulated using an elastic-plastic–creep finite-element stress model. A primary thermal-creep law for the Cu-0.28 pct Al$_2$O$_3$ copper alloy was found by fitting the four-point-bending fatigue tests. The ratchetting displacements and local depressions predicted using this equation in an elastic-plastic-creep model approximately matched those from the fatigue test results.

No attempt was made to extract a failure correlation from the present data, because the failure mechanisms are believed to be too complex for a simple correlation to be reasonably be extrapolated from them. Cracks sometimes ran to the interface and then turned to run along the interface. At other times, the cracks ran to the neutral axis of the specimen, before arresting or turning. The relationship between the location of the neutral axis of the specimen to the interface

between layers appears to be critical in understanding the failure of a layered specimen.

This combined experimental modeling approach is a powerful method to tackle complex problems. Much more work is needed on the specific problem of finding mechanical properties to enable the prediction of the thermal fatigue life of copper alloy components. Finite-element simulations of the test specimens, such as those conducted in the present work, should be routinely conducted to help analyze the results of fatigue and other complex experiments in the future.

VII. CONCLUSIONS

This article reviews quantitatively the thermal-creep laws and fatigue-lifetime correlations of the copper alloys Cu-Ag-P, Cu-Cr-Zr, Cu-Ni-Be, and Cu-Al$_2$O$_3$. This work then demonstrates how experiments and modeling should be performed together to develop property data for the analysis of complex structures.

1. Design and perform experiments where the sample geometry, material, and load conditions match as closely as possible the critical portions of the real structure of interest. In this work, four-point-bend fatigue specimens consisting of layers of copper and stainless steel are loaded sinusoidally to match typical conditions expected in high-heat-flux structures.
2. Simulate the experiments with a realistic computational model and modify the input parameters and models until the predictions match the test results. In this work, an elastic-plastic–creep finite-element model is applied and a new power-law expression is developed to describe primary creep of Cu-0.28 pct Al$_2$O$_3$.
3. Apply the computational model to the real complex structure of interest and use predictions such as the mechanical behavior and fatigue life to optimize the design and ensure safety. The present model is applied to simulate the mold of a continuous-casting machine and the first wall of ITER, in work described elsewhere.[2,45]

ACKNOWLEDGMENTS

APPENDIX
Analytical solution for bending in elastic region

The stress distribution calculated through the thickness of the bending-test specimen matches the following analytical solution in the linear elastic region. Based on the geometry defined in Figure 9 and assuming maximum load (P_{max} = 3.088 kN, E_{Cu} = 130 GPa, and E_{ss} = 140 GPa), the maximum stresses in the stainless steel (σ_{ss}) and copper (σ_{Cu}) are

$$\sigma_{ss} = \frac{Mh_1}{I_{eqss}} = \frac{P_{max}L'}{4}\frac{E_{ss}\,h_1}{(EI)_{eff}} = -229 \text{ MPa} \quad [A1]$$

$$\sigma_{Cu} = \frac{Mh_2}{I_{eqcu}} = \frac{P_{max}L'}{4}\frac{E_{Cu}\,h_2}{(EI)_{eff}} = +221 \text{ MPa} \quad [A2]$$

where $(EI)_{eff} = (I_{SS}\,E_{SS} + I_{Cu}\,E_{Cu}) = 2.466 \times 10^5$ GPa mm^{-4}, $I_{SS} = H_1{}^3b/12 + H_1\,(h_1 - 0.5\,H_1)^2 b = 864$ mm^4, $I_{Cu} = H_2{}^3b/12 + H_2\,(h_2 - 0.5\,H_2)^2\,b = 966$ mm^4

$$h_1 = \frac{0.5\,E_{ss}H_1^2 + E_{Cu}H_1H_2 + 0.5\,E_{Cu}H_2^2}{E_{ss}H_1 + E_{Cu}H_2} = 5.89 \text{ mm};$$
$$h_2 = H_1 + H_2 - h_1 = 6.11 \text{ mm} \quad [A3]$$

$$\delta_A = \frac{P_{max}a/2}{6\,(EI)_{eff}}\,(4\,a^2 - 3\,L'a) = 0.13 \text{ mm};$$
$$\delta_{max} = \frac{P_{max}a/2}{24\,(EI)_{eff}}\,(4\,a^2 - 3\,L'^2) = 0.15 \text{ mm} \quad [A4]$$

In the elastic region, the vertical displacement (δ) is directly proportional to the load, so their ratio, the theoretical compliance of the specimen, is a constant:

$$\left|\frac{\delta_A}{P_{max}}\right| = \left|\frac{(4\,a - 3\,L')a^2}{12\,(EI)_{eff}}\right| = 4.21 \times 10^{-8} \text{ m N}^{-1} \quad [A5]$$

REFERENCES

1. B.G. Thomas: "Effect of Copper Properties on Thermal Distortion of Continuous Slab Casting Molds," University of Illinois at Urbana–Champaign, Urbana, IL, Report to Brush Wellman, Cleveland, OH; August 26, 1993.
2. B.G. Thomas, G. Li, A. Moitra, and D. Habing: *ISS Trans.*, 1998, vol. 25(10), pp. 125-43.
3. J.O. Ratka and W.D. Spiegelberg: *IEEE Trans. Magn.*, 1994, vol. 30(4), pp. 1859-62.
4. T.G. O'Connor and J.A. Dantzig: *Metall. Mater. Trans. B*, 1994, vol. 25B, pp. 443-57.
5. S.J. Zinkle and S.A. Fabritsev: *Atomic and Plasma-Material Interaction Data for Fusion*, December 1994, vol. 5, pp. 163-191.
6. J.F. Stubbins, D.C. Drockelman, P. Kurath, K.D. Leedy, G. Li, J.L. McAfee, G.D. Morgan, K.T. Stattery, B.G. Thomas, and G.W. Willy: Report No. ITER/US/95/IV-BL-20, Final Report of U.S. ITER Task T8 (CY 1995), University of Illinois at Urbana–Champaign,Urbana, IL, Dec. 1995.
7. P. Fenici, D.J. Boerman, G.P. Tartaglia, and J.D. Elen: *J. Nucl. Mater.*, 1994, vols. 212–215, pp. 399-403.
8. I.V. Gorynin, S.A. Fabritsiev, and V.V. Rybin: *J. Nucl. Mater.*, 1992, vols. 191–194, pp. 401-06.
9. R.J. Weggel, J.O. Ratka, W.D. Spiegelberg, and Y. Sakai: *IEEE Trans. Magn.*, 1994, vol. 30 (4), pp. 2188-91.
10. "Elbrodur Cu-Cr-Zr Alloys," Technical Data Brochure on Cu Alloy Moulds for Continuous Casting, KM Europa-Metal (Kabelmetal), Oshabruck, Germany, Mar. 1997.
11. R.R. Solomon, A.V. Nadkarni, and J.D. Troxell: University of Illinois at Urbana–Champaign, Urbana, IL, personal communication, Oct. 3, 1995.
12. J.-P. Blanchet: *Rev. Metall.-CIT*, 1982, vol. 82, pp. 237-52.
13. P.F. Kozlowski, B.G. Thomas, J.A. Azzi, and H. Wang: *Metall. Trans. A*, 1992, vol. 23A, pp. 903-18.
14. L. Shi and D.O. Northwood: *J. Mater. Eng. Performance*, 1995, vol. 4 (2), pp. 196-211.
15. S.J. Zinkle: Report No. DOE/ER-0045/16, Department of Energy, Oak Ridge National Laboratory, Oak Ridge, TN, Mar. 31, 1986, pp. 164-67.
16. J.E. Synk and K. Vedula: *Mater. Sci. Technol.*, 1987, vol. 3, pp. 72-75.
17. J.J. Stephen and D.T. Schmale: Report No. SAND87-1296, Sandia National Laboratories, Albuquerque, NM, 1987.
18. J.J. Stephen, R.J. Bourcier, F.J. Vigil, and D.T. Schmale: Report No. SAND88-1351, Sandia National Laboratories, Albuquerque, NM, 1988.
19. V.R. Barabash, G.L. Saksugansky, Y.F. Shevakin, *et al.*: ITER-IL-NE-

1-0-3, ITER Joint Central Team, San Diego JWS, La Jolla, CA, USA, Feb. 1990.

20. T.J. Miller, S.J. Zinkle, and B.A. Chin: *J. Nucl. Mater.*, 1991, vols. 179–181, pp. 263-66.
21. H. Gravemann: "Materials for Mold Liners for Continuous Casting of Steel Present Position and Latest Trends," Presented at the Duisburger StranggieBstage, London, 1984.
22. W. Vandermeulen, V. Massaut, J.V.D. Velde, and W. Hendrix: *Proc. 14th Symp. on Fusion Technology*, Pergamon Press, New York, NY, 1986, pp. 1031-35.
23. S.V. Raj and T.G. Langdon: *Acta Metall.*, 1988, vol. 37 (3), pp. 843-52.
24. M.S. Nagorka, G.E. Lucas, and C.G. Levi: *Metall. Mater. Trans. A*, 1995, vol. 26A, pp. 873-82.
25. S.E. Broyles, K.R. Anderson, J.R. Groza, and J.C. Gibeling: *Metall. Mater. Trans. A*, 1996, vol. 27A, pp. 1217-27.
26. A. Ayensu and T.G. Langdon: *Metall. Mater. Trans. A*, 1996, vol. 27A, pp. 901-07.
27. M.A. Morris and J.C. Joye: *Acta Mater.*, 1995, vol. 43 (1), pp. 69-81.
28. C. Dubois and M.A. Morris: *Scripta Metall. Mater.*, 1994, vol. 30 (7), pp. 827-32.
29. W.D. Nix and J.C. Gibeling: *Flow and Fracture at Elevated Temperature*, ASM, Metals Park, OH, 1985.
30. P.W. Taubenlat, W.E. Smith, and A.R. Graviano: *High Conductivity Copper and Aluminum Alloys*, TMS-AIME, Warrendale, PA, 1984, pp. 19-29.
31. J. Robles, K.R. Anderson, J.R. Groza, and J.C. Gibeling: *Metall. Mater. Trans. A*, 1994, vol. 25A, pp. 2235-45.
32. T.S. Srivatsan, S. Anand, and J.D. Troxell: *Eng. Fract. Mech.*, 1993, vol. 46 (2), pp. 183-98.
33. *ABAQUS User's Manual*, K. Hibbitt, and Sorensen, Inc., Providence, RI, 1997.
34. O.C. Zienkiewicz: *The Finite Element Method*, 3rd ed., McGraw-Hill Book Company Limited, New York, NY, 1984.
35. S. Suresh: *Fatigue of Materials*, Cambridge University Press, Cambridge United Kingdom, 1991, p. 617.
36. S.S. Manson: Report No. 1170, National Advisory Commission on Aeronautics, Lewis Flight Propulsion Laboratory, Cleveland.
37. S.S. Manson and G.R. Halford: *Int. J. Fract.*, 1981, vol. 17, pp. 169.
38. L.F. Coffin: *Trans. ASME*, 1954, vol. 76, pp. 931-50.
39. H. Sehitoglu: "Thermal Mechanical Fatigue Life Prediction Methods," ASTM STP, 1990, vol. 1122, pp. 47-77.
40. J.F. Stubbins, P. Kurath, D. Drockelman, G.D. Morgan, J. McAfee, G. Li, and B.G. Thomas: *1995 16th IEEE/NPSS Symp. on Fusion Engineering*, University of Illinois at Urbana–Champaign, Urbana, IL, 1995, pp. 174-77.
41. K.D. Leedy and J.F. Stubbins: University of Illinois at Urbana–Champaign, Urbana, IL, private communication, June 1996.
42. B.E. Jelke: Master's Thesis, University of Illinois at Urbana–Champaign, Urbana, IL, 1989.
43. K. Hatanaka and Y. Ishimoto: *Proc. 1992 Joint ASME/JSME Conf. on Electronic Packaging*, Milpitas, CA, ASME, New York, NY, 1992, pp. 813-18.
44. M.C. Billone: Report No. DOE/ER-0313/19, Fusion Reactor Material Semiannual Progress Report Argonne National Laboratory, Argonne, IL, Dec. 31, 1995, p. 295.
45. G. Li: Ph.D. Thesis, University of Illinois at Urbana–Champaign, Urbana, 1996.